Converging spherical and cylindrical elastic–plastic waves of small amplitude

Hu Qiu-Shi(胡秋实)† and Zhao Feng(赵 锋)

Laboratory for Shock Wave and Detonation Physics Research, Institute of Fluid Physics, China Academy of Engineering Physics, Mianyang 621900, *China*

(Received 9 January 2014; revised manuscript received 20 February 2014; published online 23 July 2014)

Converging spherical and cylindrical elastic–plastic waves in an isotropic work-hardening medium is investigated on the basis of a finite difference method. The small amplitude pressure is applied instantaneously and maintained on the outer surface of a spherical or a cylindrical medium. It is found that for undercritical loading, the induced wave structure is an elastic front followed in turn by an expanding plastic region and an expanding elastic region. For supercritical loading, the elastic front is followed in turn by an expanding plastic region, a narrowing elastic region and an expanding plastic region. After yielding is initiated, the strength of the elastic front is constant and equal to the critical loading pressure. The motion of the continuous elastic–plastic interface is discussed in detail. Spatial distributions of pressure near the axis show the strength of the converging wave is nearly doubled in the reflecting stage.

Keywords: converging waves, spherical waves, cylindrical waves, elastic–plastic waves

PACS: 62.20.F– **DOI:** 10.1088/1674-1056/23/9/096202

1. Introduction

The diverging spherical and cylindrical elastic–plastic waves induced by loading at a circular cavity have been widely investigated by many researchers, both analytically and numerically.[1–10] Morland developed a linearized theory to determine the global solutions for diverging spherical elastic–plastic waves in terms of wave functions.[1] For instantaneous loading, Chadwick and Morland have obtained explicit forms of those wave functions in which the elastic–plastic interface is discontinuous and propagates at a pre-determined speed.[2] Morland carried out a closed-form solution for instantaneous loading and smooth unloading.[3] An explicit solution was obtained by prescribing the attenuation of the plastic loading front. The initiation of elastic–plastic interfaces is investigated in Refs. [4]–[6]. Milne *et al*. constructed a solution for continuous loading.[7] The motion of the continuous elastic–plastic interface is part of the solution to be determined. In contrast to the diverging elastic–plastic waves mentioned above, investigations on converging waves were mainly focused on gas, fluid but not elastic–plastic materials.[11–17] Bach *et al*. has obtained analytical solutions for the initial phases of the collapse of the converging spherical or cylindrical shock wave in a perfect gas.[11] Sod introduced a numerical procedure to solve the one-dimensional equations of gas dynamics for a converging cylindrical or spherical flow,[13] in which the assumption of inviscid and no-heat-conducting is used. By a theoretical study of the singular points of a set of three ordinary differential equations, Chisnell R F provided a simple analytic description of the flow behind collapsing shock waves.[14] For converging shock waves in solids, Hiroe *et al.* constructed a Riemann solver for the solids with the Gruneisen-type equation of state. The solver needs no iteration in the classification of three flow patterns which appear in the generalized Riemann problem and is incorporated into the random choice method.[16]

The purpose of this paper is mainly to carry out the converging spherical and cylindrical elastic–plastic wave structures and analyze the motion of the continuous elastic–plastic interface. The source of the waves is a small amplitude pressure applied suddenly and maintained on the outer surface of a spherical or a cylindrical medium. The material is assumed to be rate-independent, isotropic work hardening and obeying the von Mises yield condition. Basic equations for spherical and cylindrical waves are provided in Section 2. The calculation results for spherical waves are presented in Sections 3.1 and 3.2. It should be mentioned here that after yielding is initiated, the elastic front will keep a constant strength which is equal to the critical loading pressure. The motion of the continuous elastic–plastic interface is investigated in detail. The cases of cylindrical waves are presented in Section 3.3. It can be seen that except r_Y where yielding is initiated, the wave structure of the cylindrical wave is similar to that of the spherical wave. Finally, spatial distributions of pressure in the reflecting stage are given in Section 3.4.

2. Governing equations and constitutive relations

For spherical polar coordinate (r,θ,φ), the principal stress σ, strain ε, and strain rate $\dot{\varepsilon}$ are[7]

$$\begin{cases} \sigma_r = \sigma_r(r,t), \quad \sigma_\theta(r,t) = \sigma_\varphi(r,t), \\ \varepsilon_r = \varepsilon_r(r,t), \quad \varepsilon_\theta(r,t) = \varepsilon_\varphi(r,t), \\ \dot{\varepsilon}_r(r,t) = \dfrac{\partial v(r,t)}{\partial r}, \quad \dot{\varepsilon}_\theta(r,t) = \dot{\varepsilon}_\varphi(r,t) = \dfrac{v(r,t)}{r}. \end{cases} \tag{1}$$

†Corresponding author. E-mail: hhqxsr@mail.ustc.edu.cn

© 2014 Chinese Physical Society and IOP Publishing Ltd

For cylindrical polar coordinate (r,θ,z), the principal stress, strain, and strain rate are[18]

$$\begin{cases} \sigma_r = \sigma_r(r,t), \quad \sigma_\theta = \sigma_\theta(r,t), \quad \sigma_z = \sigma_z(r,t), \\ \varepsilon_r = \varepsilon_r(r,t), \quad \varepsilon_\theta = \varepsilon_\theta(r,t), \quad \varepsilon_z(r,t) = 0, \\ \dot{\varepsilon}_r(r,t) = \dfrac{\partial v(r,t)}{\partial r}, \quad \dot{\varepsilon}_\theta(r,t) = \dfrac{v(r,t)}{r}, \quad \dot{\varepsilon}_z(r,t) = 0, \end{cases} \tag{2}$$

where $v(r,t)$ is radial velocity. Radial mass balance is given by

$$\begin{cases} \rho_0 R^2 \mathrm{d}R = \rho r^2 \mathrm{d}r, & \text{spherical}, \\ \rho_0 R \mathrm{d}R = \rho r \mathrm{d}r, & \text{cylindrical}, \end{cases} \tag{3}$$

where R and r are the Lagrange and Euler coordinates, respectively, ρ_0 and ρ are the initial and transient densities. The radial momentum balance, in the absence of body force, is given by

$$\begin{aligned} &\frac{\partial[-(p+q)+s_r]}{\partial R} + n_0 \frac{s_r - s_\theta}{R} = \rho_0 \frac{\partial v}{\partial t}, \\ &n_0 = \begin{cases} 2, & \text{spherical}, \\ 1, & \text{cylindrical}, \end{cases} \end{aligned} \tag{4}$$

where p is the hydrostatic pressure, s_r and s_θ are deviator stresses, and q is the artificial viscosity

$$q = \begin{cases} \rho L[c_0 L(\dot{\varepsilon}_V)^2 - c_1 c_K \dot{\varepsilon}_V], & \dot{\varepsilon}_V < 0, \\ 0, & \dot{\varepsilon}_V \geq 0, \end{cases} \tag{5}$$

where c_0, c_1 are artificial viscosity coefficients, c_K is the bulk wave speed, and $\dot{\varepsilon}_V$ is the bulk strain rate

$$\dot{\varepsilon}_V = \begin{cases} \dfrac{1}{3}(\dot{\varepsilon}_r + 2\dot{\varepsilon}_\theta), & \text{spherical}, \\ \dfrac{1}{3}(\dot{\varepsilon}_r + \dot{\varepsilon}_\theta), & \text{cylindrical}. \end{cases} \tag{6}$$

For small amplitude loading and assuming no plastic volume change, the dilatation law in both elastic and plastic regions is

$$\sigma_r(r,t) + n_0 \sigma_\theta(r,t) + n_1 \sigma_z(r,t) = 3K(\varepsilon_r + n_0 \varepsilon_\theta), \tag{7}$$

where $n_0 = 2$; $n_1 = 0$ and $n_0 = 1$; $n_1 = 1$ for spherical and cylindrical waves, respectively.

For elastic changes, inside or unloading from the yield surface, there are shear laws

$$\begin{cases} \mathrm{d}s_r = 2G\mathrm{d}e_r, \\ \mathrm{d}s_\theta = \mathrm{d}s_\varphi = 2G\mathrm{d}e_\theta, \end{cases} \quad \text{spherical},$$

$$\begin{cases} \mathrm{d}s_r = 2G\mathrm{d}e_r, \\ \mathrm{d}s_\theta = 2G\mathrm{d}e_\theta, \\ \mathrm{d}s_z = 2G\mathrm{d}e_z, \end{cases} \quad \text{cylindrical}. \tag{8}$$

For plastic loading, assuming rate-independent and isotropic work hardening, the yield condition becomes

$$\bar{\sigma} = \bar{\sigma}(\bar{\varepsilon}_\mathrm{p}) = Y_0 + B\bar{\varepsilon}_\mathrm{p}^N, \tag{9}$$

where Y_0 is the initial yield stress, B and N are strain hardening coefficients, and $\bar{\varepsilon}_\mathrm{p}$ is the effective plastic strain. Let the trial stress status be defined as s_r^*, $s_\theta^* = s_\varphi^*$ for spherical waves and s_r^*, s_θ^*, s_z^* for cylindrical waves, using the radius regression method proposed in Ref. [19], the true stress status is obtained

$$s_{\mathrm{ii}} = (\bar{\sigma}/\sigma^*)s_{\mathrm{ii}}^*, \tag{10}$$

where ii are r, θ and r, θ, z for spherical and cylindrical waves respectively, $\bar{\sigma}$ and σ^* are the effective stress of the true stress status and the trial stress status. The finite difference method is used to discretize the above governing equations and constitutive relations. The calculation process is similar to Ref. [20], which is not stated here in detail. According to Fig. 1, the radius a is set to be 0.1 m. A uniform pressure denoted by p_0 is applied instantaneously and maintained on the outer surface of a spherical or a cylindrical medium. The mass density is 2770 kg/m^3, the shear and bulk moduli are 27.6 GPa and 78.6 GPa respectively. The work hardening case with $Y_0 = 337$ MPa, $B = 343$ MPa, and $N = 0.41$ is investigated. According to Refs. [2] and [3], the critical loading pressure is

$$p_{\mathrm{cr}} = -Y_0\left(\frac{K}{2G} + \frac{2}{3}\right). \tag{11}$$

According to Eq. (11), four cases with different forms of wave structures and interface motions are presented in the following sections.

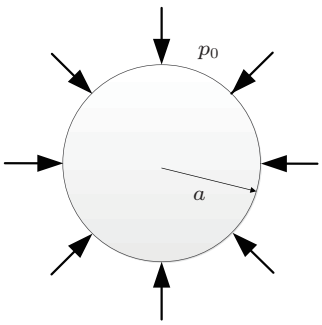


Fig. 1. Spherical and cylindrical loading for $\sigma_r(a,t) = p_0$.

3. Calculation results

3.1. Spherical undercritical loading ($|p_0| < |p_{\mathrm{cr}}|$)

From Figs. 2(a) and 2(b), it is observed that before $t_Y = 7.87$ μs at which yielding is initiated, a discontinuous elastic front propagates with an increasing strength toward the center. At $t_Y = 7.87$ μs, yielding is initiated, then the elastic front will propagate continuously with a constant strength denoted by p_{con}, followed by a slower continuous elastic–plastic interface. The two dashed vertical parallels of each time in Fig. 2 denote the elastic front and elastic–plastic interface respectively, the whole radius of each time is divided into three regions, the elastic front region E_1, followed by the plastic loading region P_1, in turn followed by the elastic region E_2.

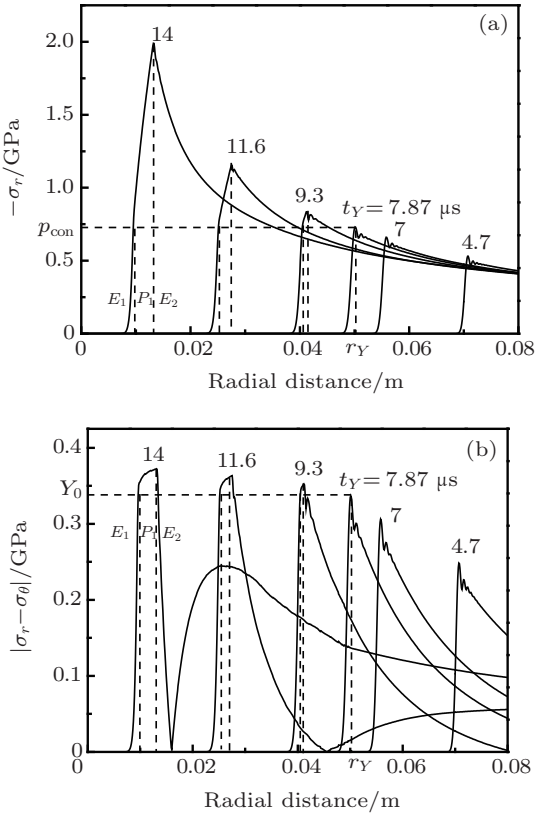


Fig. 2. Spherical converging elastic–plastic wave structure for $p_0 = p_{cr}/2$. (a) Radial stress versus the radial distance. (b) Effective stress versus the radial distance.

It should be noted that along the continuous elastic–plastic interface bounded by P_1 and E_2, both the radial stress σ_r and effective stress $|\sigma_r - \sigma_\theta|$ reach their peak values. Furthermore, as time goes on, the radial distance between elastic front and elastic–plastic interface becomes larger, resulting in an expanding plastic loading region P_1. From Ref. [5], the speed of continuous elastic–plastic interface λ bounded by P_1 and E_2 is governed by

$$\frac{\partial|\sigma_r-\sigma_\theta|_p}{\partial|\sigma_r-\sigma_\theta|_e}{\partial t} = \left(\frac{\frac{\lambda^2}{c_L^2}-1}{\frac{\lambda^2}{c_p^2}-1}\right)\left(\frac{2(1-\upsilon)\beta}{1+(1-2\upsilon)\beta}\right), \quad (12)$$

where the subscripts e and p denote the evaluations of effective stress $|\sigma_r - \sigma_\theta|$ in the elastic and plastic regions respectively, c_p is the plastic wave speed, υ is the Poisson ratio, and β is related to the work hardening rate and is in the range of [0,1]. According to Fig. 2(b), we can obtain

$$\frac{\partial|\sigma_r-\sigma_\theta|_p}{\partial t} > 0, \quad \frac{\partial|\sigma_r-\sigma_\theta|_e}{\partial t} < 0. \quad (13)$$

Using Eqs. (12) and (13), $\left(\lambda^2/c_L^2-1\right)/\left(\lambda^2/c_p^2-1\right) < 0$ is obtained, hence, $c_p < \lambda < c_L$ or $c_L < \lambda < c_p$. As shown in Fig. 2(a), the maximum of radial stress is within 5 GPa. In this range, the shear modulus and flow stress will not change much as pressure and temperature increase,[21–27] which leads to $c_p < c_L$, thus

$$c_p < \lambda < c_L. \quad (14)$$

Therefore, the continuous elastic–plastic interface will propagate at a speed λ less than elastic wave speed c_L, which validates the expanding of plastic region P_1, as shown in Fig. 2. In elastic region E_2, the radial stress σ_r decreases monotonously from its peak value to boundary pressure p_0, while the effective stress $|\sigma_r - \sigma_\theta|$ firstly reduces to zero and then increases to a maximum that will not exceed the yield stress Y_0. However, if boundary pressure p_0 is larger than critical loading pressure p_{cr}, the maximum of effective stress in elastic region E_2 would exceed the yield stress and another new elastic–plastic interface begins to emerge. This will be discussed in the next section.

3.2. Spherical supercritical loading ($|p_0| > |p_{cr}|$)

It can be seen from Figs. 3(a) and 3(b) that yielding is initiated at $t = 0$ μs, then a discontinuous elastic front propagates with a constant strength p_{con} toward the center, followed by a slower continuous elastic–plastic interface. The two dashed vertical parallels of each time in Figs. 3(a) and 3(b) denote the elastic front and elastic–plastic interface respectively, similar expanding is found in plastic loading region P_1.

However, owing to strong converging effects, the effective stress $|\sigma_r - \sigma_\theta|$ in elastic region E_2 firstly reduces to zero and then increases to a magnitude which exceeds the yield stress, as shown in Figs. 3(b) and 3(c). Then, another new elastic–plastic interface forms. The dotted vertical lines of each time in Fig. 3(c) denote the new continuous elastic–plastic interfaces, while the two dashed parallels have the same definition to that shown in Figs. 3(a) and 3(b). The three vertical lines of each time divide the whole radius into four regions, the elastic front region E_1, followed by a plastic loading region P_1, in turn followed by an elastic region E_2, and a plastic region P_2. The capital and lower case forms of E_i and P_i in Fig. 3(c) denote wave structures at $t = 13.2$ μs and $t = 9.3$ μs, respectively.

It can be seen from Fig. 3(c) that as time increases, the elastic region E_2 (e_2) bounded by two elastic–plastic interfaces becomes narrower, while the plastic region P_2 (p_2) expands. The speeds of the elastic–plastic interfaces bounded by P_1, E_2 (p_1, e_2), and E_2, P_2 (e_2, p_2) are λ_a, λ_b respectively. According to Fig. 3(b), we can obtain

$$\frac{\partial|\sigma_r-\sigma_\theta|_p}{\partial t} > 0, \quad \frac{\partial|\sigma_r-\sigma_\theta|_e}{\partial t} > 0. \quad (15)$$

By using Eqs. (12) and (15), $\left(\lambda_b^2/c_L^2-1\right)/\left(\lambda_b^2/c_p^2-1\right) > 0$ is obtained, so $\lambda_b > c_L$ or $\lambda_b < c_p$. Supposing $\lambda_b < c_p$ and according to Eq. (14), then $c_p < \lambda_a < c_L$, hence, $\lambda_b < \lambda_a$. However, it can be seen from Fig. 3(c) that narrowing is found in

elastic region E_2, which means $\lambda_b > \lambda_a$. Conflict appears, thus

$$\lambda_b > c_{\rm L}. \tag{16}$$

It should be noted from Fig. 3(c) that within 3.9 μs, the elastic front of speed $c_{\rm L}$ bounded by E_1, P_1 (e_1, p_1) travels about 0.025 mm, while the elastic–plastic interface of speed λ_b bounded by E_2, P_2 (e_2, p_2) travels about 0.05 mm larger than 0.025 mm, which validates Eq. (16).

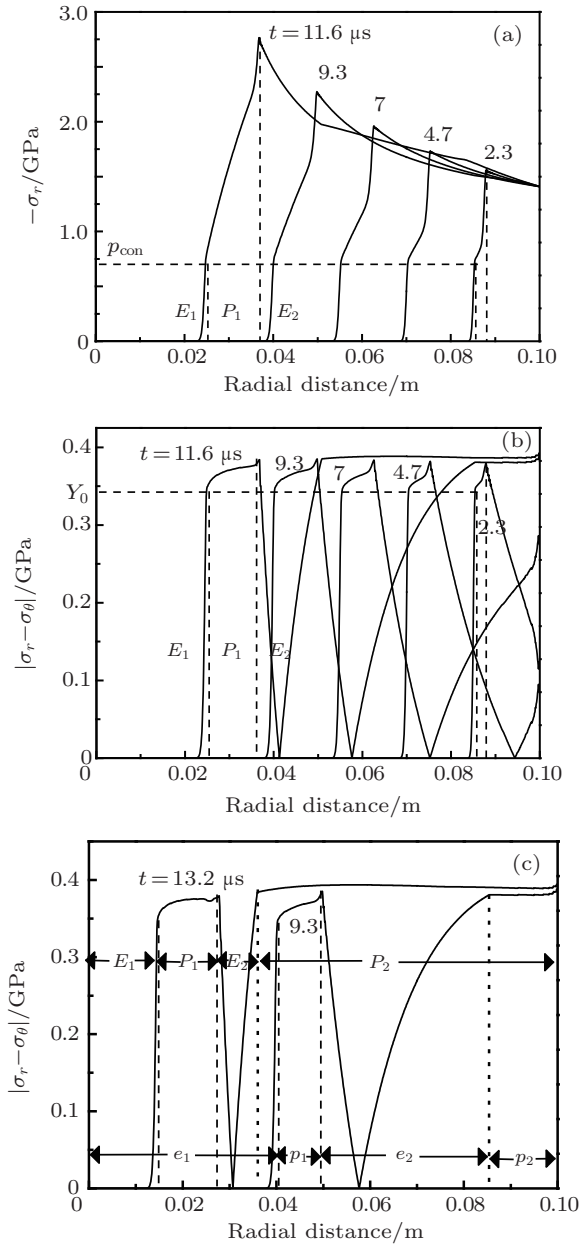


Fig. 3. Spherical converging elastic–plastic wave structure for $p_0 = 2p_{\rm cr}$. (a) Radial stress versus radial distance, (b) effective stress versus radial distance, and (c) narrowing of elastic region E_2.

The wave structures $E_1 \leftarrow P_1 \leftarrow E_2$ and $E_1 \leftarrow P_1 \leftarrow E_2 \leftarrow P_2$ in Figs. 2 and 3(c) can also be interpreted from the plastic strain versus the time histories in Fig. 4. It is observed that for undercritical loading, the effective plastic strain has a jump from 0 to 0.0015 at $t = 11$ μs, while for supercritical loading, it has jumps at $t = 12.8$ μs and $t = 13.8$ μs respectively, which further validates the wave structures as illustrated in Figs. 2 and 3.

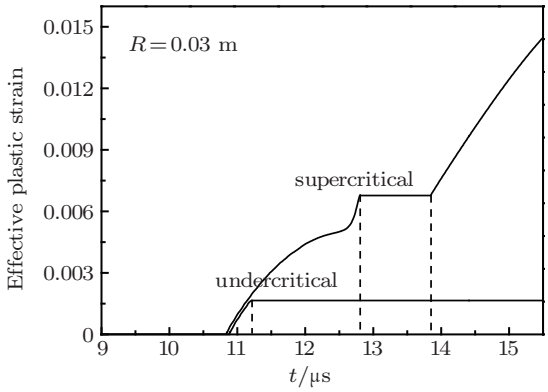


Fig. 4. Effective plastic strain versus time at $R = 0.03$ m for spherical converging elastic–plastic waves.

3.3. Cylindrical undercritical and supercritical loading

Figure 5 shows a similar wave structure as shown in Fig. 2. The wave structure $E_1 \leftarrow P_1 \leftarrow E_2$ and the expanding plastic loading region P_1 are found as well.

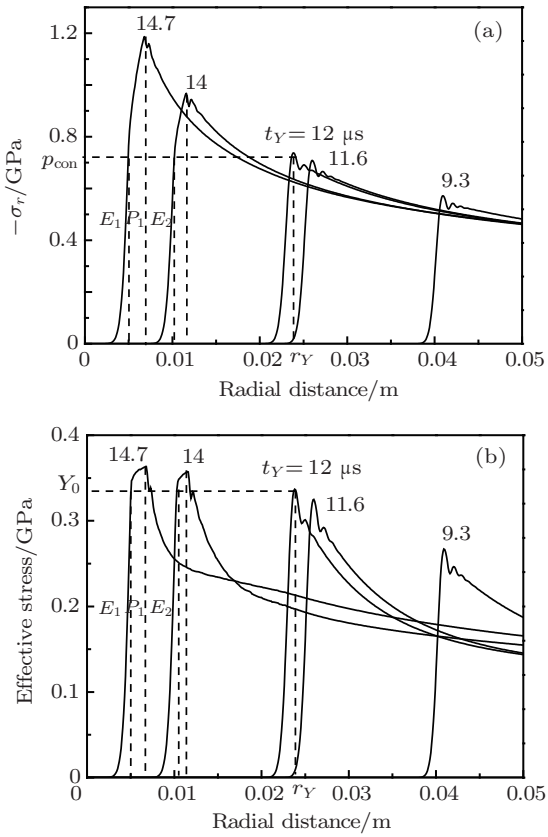


Fig. 5. Cylindrical converging elastic–plastic wave structures for undercritical loading $p_0 = p_{\rm cr}/2$. (a) Radial stress versus radial distance, (b) effective stress versus radial distance.

The most outstanding difference is the position r_Y where yielding is initiated. From Figs. 2 and 5, r_Y is approximately $a/2$ and $a/4$ respectively. From Ref. [18], before yielding is initiated, the strength of the discontinuous elastic front, the

corresponding hoop and normal stress are $\sigma_r = ap_0/r$, $\sigma_\theta = \sigma_\varphi = \upsilon\sigma_r/(1-\upsilon)$ for spherical waves and $\sigma_r = p_0\sqrt{a/r}$, $\sigma_\theta = \sigma_z = \upsilon\sigma_r/(1-\upsilon)$ for cylindrical waves. Let $\bar{\sigma} = Y_0$, thus

$$\begin{aligned} r_Y &= a|p_0/p_{\rm cr}|, \quad \text{spherical}, \\ r_Y &= a(p_0/p_{\rm cr})^2, \quad \text{cylindrical}. \end{aligned} \tag{17}$$

Since $p_0 = p_{\rm cr}/2$ in Figs. 2 and 5, according to Eq. (17), $r_Y = a/2$ and $r_Y = a/4$ are obtained respectively. Figure 6 shows a similar wave structure to that shown in Fig. 3. The expanding of plastic loading region P_1 and narrowing of elastic region E_2 are found as well. Similar to what is shown in Fig. 4, the wave structure $E_1 \leftarrow P_1 \leftarrow E_2$ in Fig. 5 and $E_1 \leftarrow P_1 \leftarrow E_2 \leftarrow P_2$ in Fig. 6(c) can also be validated from plastic strain-time histories in Fig. 7.

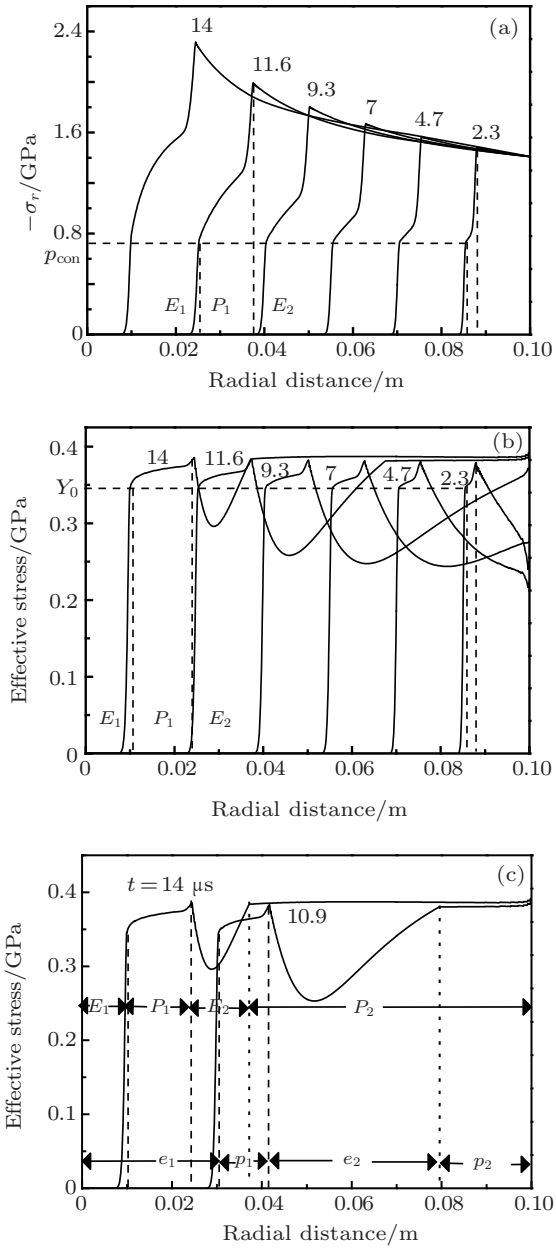


Fig. 6. Cylindrical converging elastic–plastic wave structures for supercritical loading $p_0 = 2p_{\rm cr}$. (a) Radial stress versus radial distance, (b) effective stress versus radial distance, (c) narrowing of elastic region E_2.

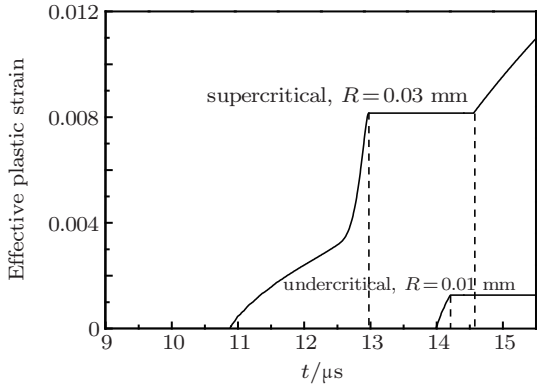


Fig. 7. Effective plastic strain versus time for cylindrical converging elastic–plastic waves.

Referring to Figs. 2(a) and 6(a), it is clear that the strength of the elastic front $p_{\rm con}$ is almost 0.7 GPa in all cases, which is very close to critical loading pressure $p_{\rm cr}$ denoted by Eq. (11). From Refs. [5] and [6], if the state of stress across any shock wave is elastic, then the discontinuity $[\boldsymbol{w}]$ is

$$[\boldsymbol{w}] = \gamma r^{\rm e}, \tag{18}$$

where $[\boldsymbol{w}]$ is

$$\boldsymbol{w} = \begin{bmatrix} v \\ \sigma_r \\ \sigma_\theta \end{bmatrix}, \quad \text{spherical}, \quad \boldsymbol{w} = \begin{bmatrix} v \\ \sigma_r \\ \sigma_\theta \\ \sigma_z \end{bmatrix}, \quad \text{cylindrical}, \tag{19}$$

where γ is a proportional factor which depends on the distance along the shock wave, $r^{\rm e}$ is right eigenvector[5,6]

$$\begin{aligned} r &= \begin{bmatrix} 1 \\ \rho c_{\rm L} \\ \rho c_{\rm L}\Phi \end{bmatrix}, \quad \text{spherical}, \\ r &= \begin{bmatrix} 1 \\ \rho c_{\rm L} \\ \rho c_{\rm L}\Phi \\ \rho c_{\rm L}\Phi \end{bmatrix}, \quad \text{cylindrical}, \end{aligned} \tag{20}$$

where $c_{\rm L}$ is elastic wave speed, Φ is $\upsilon/(1-\upsilon)$, and υ is Poisson's ratio. Using Eqs. (18)–(20), we can obtain

$$\sigma_\theta = \sigma_r\Phi, \quad \text{spherical}, \quad \sigma_\theta = \sigma_z = \sigma_r\Phi, \quad \text{cylindrical}. \tag{21}$$

According to Eq. (21) and $\bar{\sigma} = Y_0$, thus for both spherical and cylindrical waves

$$p_{\rm con} = p_{\rm cr}, \tag{22}$$

which indicates that after yielding is initiated, the strength of the elastic front is constant and equal to the critical loading pressure.

3.4. Reflecting at the axis

Calculation results are presented in Fig. 8. Two curves are shown. The solid and dashed lines denote the spatial distributions of radial stress before and after reflecting, respectively. It can be seen that for both spherical and cylindrical converging waves, the strength is nearly doubled in the reflecting stage.

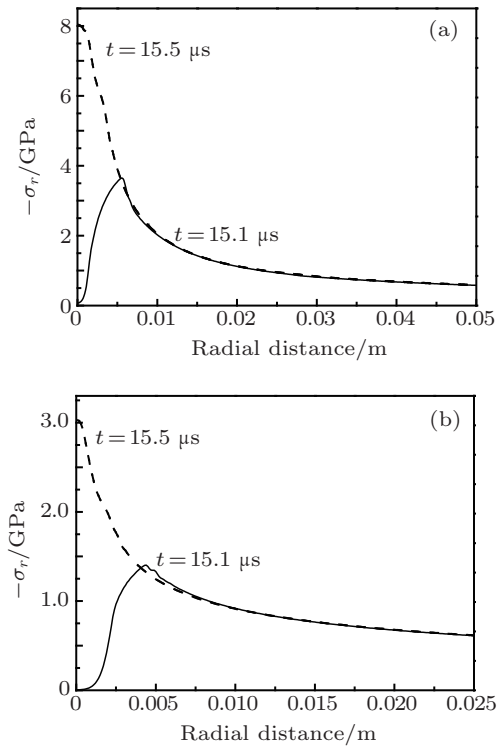


Fig. 8. Spherical (a) and cylindrical (b) reflecting at the axis for $p_0 = p_{cr}/2$.

4. Conclusion

Converging spherical and cylindrical elastic–plastic waves in an isotropic work-hardening medium are investigated in this paper. The small amplitude pressure is applied instantaneously and maintained on the outer surface of a spherical or cylindrical medium. Four important features of the converging wave structures are found.

1) For undercritical loading, the induced wave structure is $E_1 \leftarrow P_1 \leftarrow E_2$, which means that an elastic front is followed in turn by an expanding plastic region and an expanding elastic region. The continuous elastic–plastic interface bounded by P_1, E_2 propagates at a slower speed than the elastic front.

2) For supercritical loading, the induced wave structure is $E_1 \leftarrow P_1 \leftarrow E_2 \leftarrow P_2$, which means an elastic front is followed in turn by an expanding plastic region, a narrowing elastic region, and an expanding plastic region. The continuous elastic–plastic interface bounded by P_1, E_2 propagates at a slower speed than the elastic front, while the interface bounded by E_2, P_2 propagates at a faster speed than the elastic front.

3) In all cases after yielding is initiated, the strength of the elastic front is constant and equal to the critical loading pressure. Along the continuous elastic–plastic interface bounded by P_1, E_2, both the radial stress and effective stress reach their peak values.

4) The strength of the converging wave is nearly doubled in the reflecting stage.

References

[1] Morland L W 1969 *J. Mech. Phys. Solids* **17** 371
[2] Chadwick P and Morland L W 1969 *J. Mech. Phys. Solids* **17** 419
[3] Morland L W 1970 *J. Mech. Phys. Solids* **19** 295
[4] Swift R P and Fyfe I M 1970 *J. Appl. Mech.* **37** 1134
[5] Srinivasan M G and Ting T C T 1974 *J. Mech. Phys. Solids* **22** 415
[6] Srinivasan M G and Ting T C T 1975 *Int. J. Solids Structures* **11** 1057
[7] Milne P C and Morland L W 1988 *J. Mech. Phys. Solids* **36** 215
[8] Yang C Y 1970 *Int. J. Solids Structures* **6** 757
[9] Fotiu P A and Ziegler F 1996 *Int. J. Solids Structures* **33** 811
[10] Rapoport L, Katzir Z and Rubin M B 2011 *Wave Motion* **48** 441
[11] Bach G G and Lee J H 1969 *J. Fluid Mech.* **37** 513
[12] Drikakis D, Govatsos P A and Papantonis D E 1994 *Int. J. Numer. Methods Fluids* **19** 667
[13] Sod G A 1977 *J. Fluid Mech.* **83** 785
[14] Chisnell R F 1998 *J. Fluid Mech.* **354** 357
[15] Matsuo H and Nakamura Y 1981 *J. Appl. Phys.* **52** 4503
[16] Hiroe T, Matsuo H and Fujiwara K 1992 *J. Appl. Phys.* **72** 2605
[17] Gurovich V T, Grinenko A and Krasik Y E 2007 *Phys. Rev. Lett.* **99** 124503
[18] Wang L L 2005 *Foundation of Stress Waves* **2** 232 (in Chinese)
[19] Li Y C, Tan F L, Yao L and Hu X Z 2004 *Explosion and Shock Waves* **24** 289 (in Chinese)
[20] Wang X J, Hu X Z and Li Y C 1991 *Explosion and Shock Waves* **11** 97 (in Chinese)
[21] Chen Y T, Tang X J and Li Q Z 2010 *Chin. Phys. B* **19** 056402
[22] Yu Y Y, Tan H, Hu J B and Dai C D 2008 *Chin. Phys. B* **17** 264
[23] Steinberg D J, Cochran S G and Guinan M W 1980 *J. Appl. Phys.* **51** 1498
[24] Steinberg D J 1987 *Int. J. Impact. Eng.* **5** 603
[25] Peng J X, Jing F Q, Li D H and Wang L L 2005 *J. Appl. Phys.* **98** 013508
[26] Burakovsky L and Preston D L 2005 *Phys. Rev. B* **71** 184118
[27] Nadal M H and Poac P L 2003 *J. Appl. Phys.* **93** 2472